

# Position Control for Hysteresis Motors: Transient-time Model and Field-oriented Control

Lei Zhou, *Student Member, IEEE*, Wolfgang Gruber, *Member, IEEE*, and David L. Trumper, *Member, IEEE*

**Abstract**—This paper studies the modeling and field-oriented control (FOC) for hysteresis motors, with the goal of achieving position control of hysteresis motors for servo applications. Hysteresis motors include a wide range of machines with solid cylindrical or ring-shaped steel rotors, which generate torque primarily via the magnetic hysteresis effect of the rotor material. Previously, hysteresis motors have been mainly used under open-loop operation. However, they are also attractive for position control in some special applications such as in-vacuum operation or when smooth running and high speed is required.

In this work, an equivalent circuit model for hysteresis motors that describes the motor's transient-time dynamics is introduced, and a state space model for hysteresis motors is developed. This model is used to construct a rotor flux orientation observer for the FOC for hysteresis motors. Three methods for estimating the rotor field angle are introduced. The proposed FOC-based position control method was tested with three hysteresis motors, including two custom-made motors of different rotor materials and one off-the-shelf hysteresis motor. Experimental results show that position control for all three hysteresis motors can reach a bandwidth of 130 Hz with the proposed methods. To the authors' best knowledge, this is the first experimental study on FOC and position control for hysteresis motors.

**Index Terms**—hysteresis motor, field-oriented control, motion control

## NOMENCLATURE

$i_s$	stator current
$u_s$	stator voltage
$i_{HR}$	hysteresis part of rotor apparent current
$i_{Er}$	eddy current part of rotor apparent current
$i_m$	$= i_s + i_{HR} + i_{Er}$ , magnetizing current
$\Phi_r$	rotor flux
$\Phi_{HR}$	hysteresis part of rotor flux
$\Phi_{Er}$	eddy current part of rotor flux
$\mu$	magnetic permeability
$\delta$	hysteresis lag angle
$\omega_e, \omega_r$	motor electrical and mechanical speed
$R_s, L_{ls}$	stator resistance and leakage inductance
$L_m$	mutual inductance
$R_{HR}, L_{lHR}$	hysteresis part rotor resistance and inductance
$R_{Er}, L_{lEr}$	eddy current part rotor resistance and inductance
$\hat{[]}$	denote estimated values
$[ ]_d, [ ]_q$	denote values in the rotor flux-oriented frame
$[ ]_D, [ ]_Q$	denote values in the stationary frame

L. Zhou and D. Trumper are with the Department of Mechanical Engineering, Massachusetts Institute of Technology, Cambridge, MA, 02139, USA. leizhou@mit.edu, trumper@mit.edu

W. Gruber is with the Institute of Electrical Drives and Power Electronics, Johannes Kepler University, Linz, Austria. wolfgang.gruber@jku.at.

$[ ]_d, [ ]_q$  denote values in the rotor-fixed frame  
 $I, J, \mathbf{0} = \begin{bmatrix} 1 & 0 \\ 0 & 1 \end{bmatrix}, = \begin{bmatrix} 0 & -1 \\ 1 & 0 \end{bmatrix}, = \begin{bmatrix} 0 & 0 \\ 0 & 0 \end{bmatrix}$

## I. INTRODUCTION

**A**MONG many motor drive principles, the hysteresis motor is receiving increasing attention in the past decade due to its advantages of simple structure, vibration-free operation, high rotor thermal and mechanical robustness and self-starting capability. A hysteresis motor operates using the magnetic hysteresis of its rotor material. Since the magnetization in the rotor lags behind the external magnetizing force, a torque is generated due to the stator and rotor field interactions [1].

There are a wide range of rotor materials for hysteresis motors, including tool steel, chrome and/or cobalt alloy, AlNiCo magnets, etc. As a result, the hysteresis motor encompasses a wide range of constructions. Fig. 1 shows an illustration of the motor type categorization according to the magnetic hardness of the rotor magnetic material. In this paper, we study hysteresis motors of different rotor magnetic hardness using a unified framework.

The common operation state for hysteresis motors is running asynchronously in transients and synchronously in steady-state. Typical applications for hysteresis motors include tape drives [2], pumps [3], [4], centrifuges [5], flywheels [6], [7], etc. For these operation modes, speed feedback control is typically not required, as the dynamics of a hysteresis motor are stable and robust under open-loop control. However, the open-loop dynamics of a hysteresis motor are usually relatively slow-converging and lightly damped, which makes the motor unsuitable for applications where dynamic performance is critical. This fact motivates our research for methods to control the motor's torque with high bandwidth, which is desired for some applications of hysteresis motors such as gyroscopes [8] and reaction wheels [9]. This advance can also allow hysteresis motors to be used for servo applications, which may be attractive for some special applications, such as high temperature or in-vacuum operations, and when smooth running and high speed is required. Prior work [10] studies the sensorless FOC for hysteresis motors and presents simulations of the proposed scheme. However, to our knowledge, experimental studies for FOC and position control for hysteresis motors have not yet been reported in the literature.

This paper is based on [11] and studies modeling and FOC for hysteresis motors, targeting at enabling high bandwidth torque control for hysteresis motors, and thus enabling them

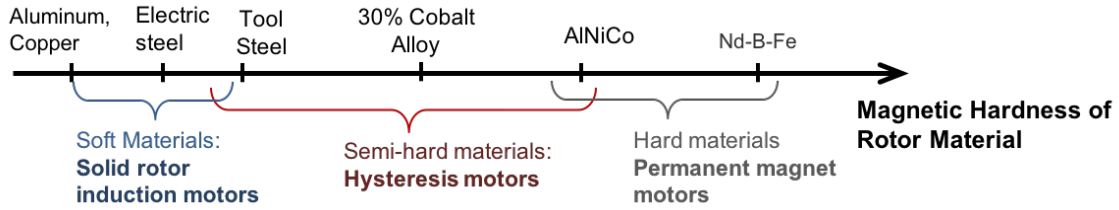


Fig. 1. Ranges of motor concepts according to the magnetic hardness of the rotor material.

being used for position servo applications. The main objectives of this paper are as follows:

- 1) Propose a novel equivalent circuit model that describes the hysteresis motor's transient-time dynamics, which can be used to design a real-time flux observer for hysteresis motors.
- 2) Introduce the FOC method for hysteresis motors, and propose several approaches for rotor flux orientation estimation.
- 3) Experimentally test the position control method on three different hysteresis motors. Experiments show that the position control based on proposed methods are successful for all three hysteresis motors.

To our knowledge, this paper presents the first experimental study for FOC and position control for hysteresis motors.

The rest of this paper is organized as follows. Section II briefly introduces the operation principles for hysteresis motors. Section III presents the modeling for hysteresis motors. Section IV focuses the FOC for hysteresis motors. Section V shows the experimental results. Conclusions and future work are outlined in Section VI.

## II. OPERATION PRINCIPLE OF HYSTERESIS MOTOR

This section briefly introduces the operation principle of hysteresis motors to make the paper self-contained. A hysteresis motor consists of a regular poly-phase stator and a rotor of solid cylindrical or ring-shaped semi-hard magnetic material. Sometimes, the semi-hard magnetic material is in a ring around an aluminum core. The magnetic hysteresis effects of the rotor material causes a lag angle between the rotor magnetic field and the air-gap magnetic field, and a hysteresis torque can be generated [1]. When the rotor of the hysteresis motor is conductive, eddy current effects also contribute to the torque generation when the motor is operating asynchronously.

Fig. 2 shows the ideal and practical hysteresis motor torque-speed curve, where  $T_m$  is the motor torque,  $\omega_m$  is the motor speed, and  $\omega_e$  is the electrical driving frequency. The ideal hysteresis motor demonstrates constant hysteresis torque during asynchronous operation, assuming the hysteresis lag angle equals its maximum when slip is non-zero. At synchronous speed, the motor torque can demonstrate different values, depending on the load torque and the motor excitation conditions. As a result, the ideal torque-speed curve demonstrates a "torque singularity" at  $\omega_m = \omega_e$ . In a practical hysteresis motor with a conductive rotor, eddy currents in rotor generate an additional slip-frequency dependent eddy current torque when in asynchronous operation, making the motor torque vary with the slip frequency. At the vicinity

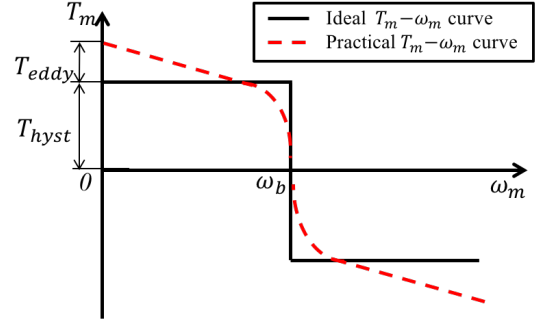


Fig. 2. Typical single-pole-pair hysteresis motor torque-speed curve. Solid blue line: ideal hysteresis motor torque-speed curve. Dashed red line: practical hysteresis motor torque-speed curve, where the effect of eddy currents is taken into account.

of synchronous speed, the practical hysteresis motor torque demonstrates smooth transition from the motoring mode to the generating mode. This is because that the hysteresis lag angle at the vicinity of synchronous speed is less than its maximum value, as is discussed in reference [12].

## III. MODELING OF THE HYSTERESIS MOTORS

### A. Time Average Model of Hysteresis Motor

This section presents the equivalent circuit model for hysteresis motors. Modeling of the hysteresis motor is challenging mainly due to the nonlinearity of hysteresis material properties. Through the years, several different models have been developed to study the motor's behavior [5], [13]–[15]. Hysteresis motors with eddy current effect being considered have been also studied [12], [14], [16], [17].

In this work, the elliptical hysteresis loop-based model for hysteresis motors proposed in [15], [16] is used to model the motor dynamics. This model has later been used in [18]–[20]. In this model, the  $B$ - $H$  curve of the rotor material is approximated by an ellipse, as  $B = B_m \cos \theta$ ,  $H = (B_m/\mu) \cos(\theta + \delta)$ , where  $B_m$  is the maximum amplitude of the flux density,  $\mu$  is the permeability of the rotor material, and  $\delta$  is the lag angle between field intensity  $H$  and flux density  $B$ . This model considers only the fundamental harmonics for  $B$ - and  $H$ -fields. By making  $\mu$  and  $\delta$  as functions of the excitation amplitude, the magnetic saturation effect can be modeled.

The elliptical hysteresis approximation allows modeling the hysteresis motor dynamics using linear circuit elements. Fig. 3 shows the hysteresis motor equivalent circuit model based on the elliptical hysteresis approximation with the eddy current effect considered developed in [16]. In this model,  $i_s$  is the stator current,  $i_m$  is the magnetizing current, and  $i_r$  is the

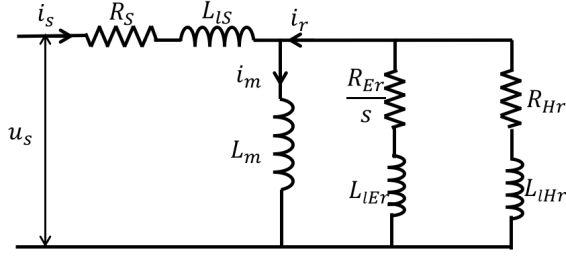


Fig. 3. Time-average per phase equivalent circuit model for hysteresis motors introduced in [16].

apparent rotor current. The values of the circuit elements can be calculated by

$$L_m = \frac{2mK_w^2 N^2 \mu_0 l r_g}{p^2 \pi g}, \quad (1)$$

$$R_{Hr} = \omega_e \frac{mK_w^2 N^2 V_r \mu}{\pi^2 r_r^2} \sin \delta, \quad (2)$$

$$L_{lHr} = \frac{mK_w^2 N^2 V_r \mu}{\pi^2 r_r^2} \cos \delta, \quad (3)$$

$$R_{Er} = \frac{l}{\rho A_h}, \quad L_{lEr} \approx 0. \quad (4)$$

Here  $K_w$  is the winding factor,  $m$  is the number of phase,  $p$  is the number of poles,  $r_r$  is mean radius of length of the magnetic field path within rotor,  $r_g$  is the mean radius of the air gap,  $\omega_e$  is the reference speed,  $N$  is the number of windings per phase per pole,  $g$  is the air-gap length,  $l$  is the rotor axial length,  $V_r$  is the effective rotor volume,  $\rho$  is the specific resistivity of the rotor material, and  $A_h$  is the effective axial cross-section area of the rotor. The stator core loss is ignored in this model. Note that this model only captures the hysteresis torque of the motor when it is operating asynchronously, which is everywhere except for the ‘‘torque singularity’’ in Fig. 2 at  $\omega_m = \omega_e$ . In order to produce a model that describes the transition from asynchronous to synchronous operation of a hysteresis motor, one needs to model the minor hysteresis loops of rotor material, which is complicated due to the nonlinearity and history-dependency of hysteresis properties. References [21] studies for the use for such a model for hysteresis motors through the finite element method.

### B. Transient-Time Dynamic Model of Hysteresis Motor

The hysteresis motor equivalent circuit model shown in Fig. 3 is a time-average model, which describes the relationships between the time-average relationships between the motor currents, fluxes and voltages. In order to design a real-time flux estimator for the motor and thus achieve a precise estimation of the rotor flux orientation, a dynamic model that describes the instantaneous current-voltage-flux relationships in a motor is needed. This model is expected to be in a form that resembles the dynamic equivalent circuit model for induction motor FOC [22], [23].

The challenge of setting up a transient-time dynamic model for hysteresis motors is mainly due to the fact that the hysteresis effect and the eddy current effect need to be modeled

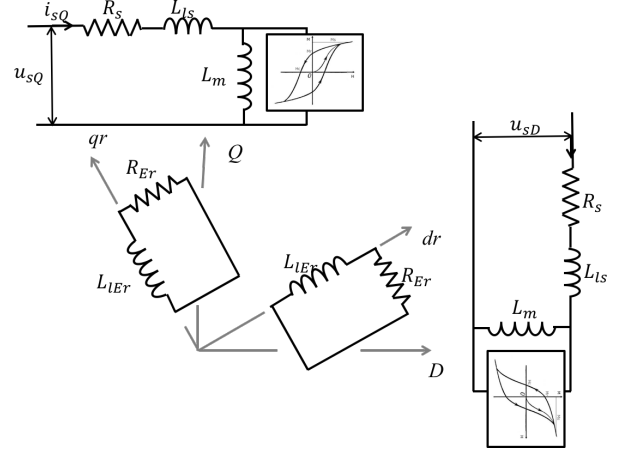


Fig. 4. Hysteresis motor circuit diagram with hysteresis effect and eddy current effect in different coordinate systems.

in different reference frames. The hysteresis effect of the rotor would cause a constant lag angle between the rotor flux and the air-gap flux, and this relationship should be modeled in the stator-fixed frame. On the other hand, the eddy current effect should be modeled in the rotor-fixed frame, since the eddy currents in the rotor are created in the conductors fixed on the rotor. This separation in reference frames is depicted in Fig. 4. This prevents us from modeling the rotor flux using unified variables as in an induction motor model.

In this work, a transient-time dynamic model for hysteresis motors with eddy current effects considered is developed. Fig. 5 shows the transient-time equivalent circuit model for the hysteresis motor in the stationary  $D-Q$  frame. In Fig. 5,  $i_s = [i_{sD}, i_{sQ}]^T$  is the stator current,  $i_{Hr} = [i_{HrD}, i_{HrQ}]^T$  is the hysteresis part rotor current, and  $i_{Er} = [i_{ErD}, i_{ErQ}]^T$  is the eddy current part rotor current. Define  $i_m = [i_{mD}, i_{mQ}]^T$  to be the magnetizing current as

$$i_m = i_s + i_{Hr} + i_{Er}. \quad (5)$$

Note that in the transient-time equivalent circuit model Fig. 5 there are rotor speed dependent voltage sources on the eddy current part of the rotor side circuits. This is because the reference frame change for the eddy current effect relationships from the rotor-fixed frame to the stationary frame. Define  $\Phi_{Hr} = [\Phi_{HrD}, \Phi_{HrQ}]^T$  and  $\Phi_{Er} = [\Phi_{ErD}, \Phi_{ErQ}]^T$  as the hysteresis part and the eddy current part of the rotor flux:

$$\Phi_{Hr} = L_m i_m + L_{lHr} i_{Hr}, \quad (6)$$

$$\Phi_{Er} = L_m i_m + L_{lEr} i_{Er}, \quad (7)$$

and the total rotor flux is defined as

$$\Phi_r = \Phi_{Hr} + \Phi_{Er} - L_m i_m. \quad (8)$$

A state space model for the hysteresis motor transient-time dynamics is derived for the model given in Fig. 4. This model is later being used to construct flux observer for the hysteresis motor in the FOC. Selecting state variable as  $x = [i_s^T, \Phi_{Hr}^T, \Phi_{Er}^T]^T = [i_{sD}, i_{sQ}, \Phi_{HrD}, \Phi_{HrQ}, \Phi_{ErD}, \Phi_{ErQ}]^T$ , the state space model for the hysteresis motor transient-time dynamics is

$$\frac{d}{dt} \begin{bmatrix} \mathbf{i}_s \\ \Phi_{Hr} \\ \Phi_{Er} \end{bmatrix} = \begin{bmatrix} -\gamma \mathbf{I} & \alpha \mathbf{I} & \beta \mathbf{I} - \frac{\sigma L_m L_{lHr} \omega_r}{\kappa} \mathbf{J} \\ \sigma R_{Hr} L_m L_{lEr} \mathbf{I} & -\sigma R_{Hr} L_{Er} \mathbf{I} & \sigma L_m R_{Hr} \mathbf{I} \\ \sigma R_{Er} L_m L_{lHr} \mathbf{I} & \sigma L_m R_{Er} \mathbf{I} & -\sigma L_{Hr} R_{Er} \mathbf{I} + \omega_r \mathbf{J} \end{bmatrix} \begin{bmatrix} \mathbf{i}_s \\ \Phi_{Hr} \\ \Phi_{Er} \end{bmatrix} + \begin{bmatrix} \frac{1}{\kappa} \mathbf{I} \\ \mathbf{0} \\ \mathbf{0} \end{bmatrix} \mathbf{u}_s \quad (9)$$

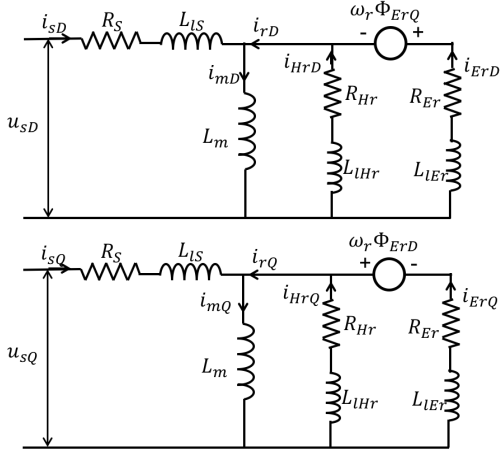


Fig. 5. Transient time equivalent circuit model for hysteresis motors including the eddy current effect in stationary  $D$ - $Q$  frame.

Here  $R_s$  is the stator resistance,  $L_m$  is the mutual inductance,  $L_{ls}$  is the stator leakage inductance,  $R_{Hr}$  and  $R_{Er}$  are the rotor side hysteresis and eddy current resistances, and  $L_{lHr}$  and  $L_{lEr}$  are the hysteresis and eddy current part rotor leakage inductances.  $L_s = L_m + L_{ls}$  is the total stator side inductance,  $L_{Hr} = L_m + L_{lHr}$  and  $L_{Er} = L_m + L_{lEr}$  are the hysteresis part and eddy current part total inductances. The rest of the parameters are defined by

$$\sigma = 1/(L_{Hr}L_{Er} - L_m^2), \quad (10)$$

$$\kappa = L_s - \sigma L_m^2 (L_{lEr} + L_{lHr}), \quad (11)$$

$$\gamma = (R_s + \sigma^2 L_m^2 (L_{lEr}^2 R_{Hr} + L_{lHr}^2 R_{Er}))/\kappa, \quad (12)$$

$$\alpha = (\sigma^2 L_m (R_{Hr} L_{Er} L_{lEr} - R_{Er} L_m L_{lHr}))/\kappa, \quad (13)$$

$$\beta = (\sigma^2 L_m (R_{Er} L_{Hr} L_{lHr} - R_{Hr} L_m L_{lEr}))/\kappa. \quad (14)$$

More details of the transient-time hysteresis motor dynamics are introduced in Appendix A.

#### IV. FIELD-ORIENTED CONTROL FOR HYSTERESIS MOTORS

The FOC for hysteresis motors is in the same kind as that of the other motor types. Fig. 6(a) shows a vector diagram of the variable relationships. In Fig. 6(a),  $D$ - $Q$  is the stationary two-phase frame, and  $d$ - $q$  is the rotor flux-oriented frame, where the  $d$ -axis is aligned with the rotor flux linkage, and the  $q$ -axis is perpendicular to the  $d$ -axis. Vector  $\mathbf{i}_s$  represents the stator phase currents, and  $\Phi_r$  is the rotor flux vector. Fig. 6(b) shows a block diagram of the position control for the hysteresis motor via FOC. In Fig. 6(b), the motor's angular position, the motor terminal currents and voltages are also measured and used to reconstruct the flux orientation through a flux orientation estimator. With the estimated rotor flux angle  $\hat{\theta}$ , the measured currents are transformed into the rotor flux-oriented

$d$ - $q$  frame and are then used for current control. The reference of  $d$ -axis current is set to be a constant. The measured motor angular position is fed-back through a position controller, and the control effort signal is set to be the reference signal for  $q$ -axis current. The two current control effort signals  $u_{sd}$  and  $u_{sq}$  are then transformed back to the stationary three-phase frame and energize the stator windings.

The most challenging element in the FOC for hysteresis motors is the rotor flux orientation estimator. The flux angle estimation accuracy directly influences the motor control performance. There are three approaches to obtain an estimate of the rotor flux angle are proposed in this paper, as introduced below.

##### A. Approximate with Motor Mechanical Angle

The simplest method to obtain an estimate for the flux angle is to directly use the measured rotor angular position, as  $\hat{\theta} = \theta_r$ , where  $\theta_r$  is the rotor's mechanical angle. This method assumes that the magnetization is fixed on the rotor surface, which resembles the case of a permanent magnet motor. Over-exciting the motor by a large  $d$ -axis current at the starting up of the motor as introduced in [24] will help improve the performance of this flux angle estimation method, as the magnetization of the rotor can be fixed along the  $d$ -axis on the rotor.

##### B. Estimate Flux via Back-EMF Measurements

The second method uses the back-electromotive force (EMF) in the stator coils to estimate the rotor flux orientation. When the magnetized rotor is rotating, the change of the rotor field will induce a voltage in the stator winding, which is the back-EMF. The back-EMF in the stationary  $D$ - $Q$  frame can be calculated as

$$\mathbf{e} = \mathbf{u}_s - R_s \mathbf{i}_s - L_{ls} \dot{\mathbf{i}}_s. \quad (15)$$

An estimate for the rotor flux linkage in the stationary two-phase frame can be calculated by

$$\hat{\Phi}_r = \int \mathbf{e} dt, \quad (16)$$

where  $\hat{\Phi}_r = [\hat{\Phi}_{rD}, \hat{\Phi}_{rQ}]^T$ . Finally the estimated flux angle  $\hat{\theta}$  can be calculated as

$$\sin \hat{\theta} = \frac{\hat{\Phi}_{rQ}}{(\hat{\Phi}_{rD}^2 + \hat{\Phi}_{rQ}^2)^{1/2}}, \quad \cos \hat{\theta} = \frac{\hat{\Phi}_{rD}}{(\hat{\Phi}_{rD}^2 + \hat{\Phi}_{rQ}^2)^{1/2}}. \quad (17)$$

This method provides good rotor flux orientation estimation performance when the motor speed is relatively high. However, when the motor is standing still or operating at low speed, the back-EMF signals are small and therefore the angle estimation is not accurate. As an alternative flux orientation estimation approach, a combination of the back-EMF based estimation

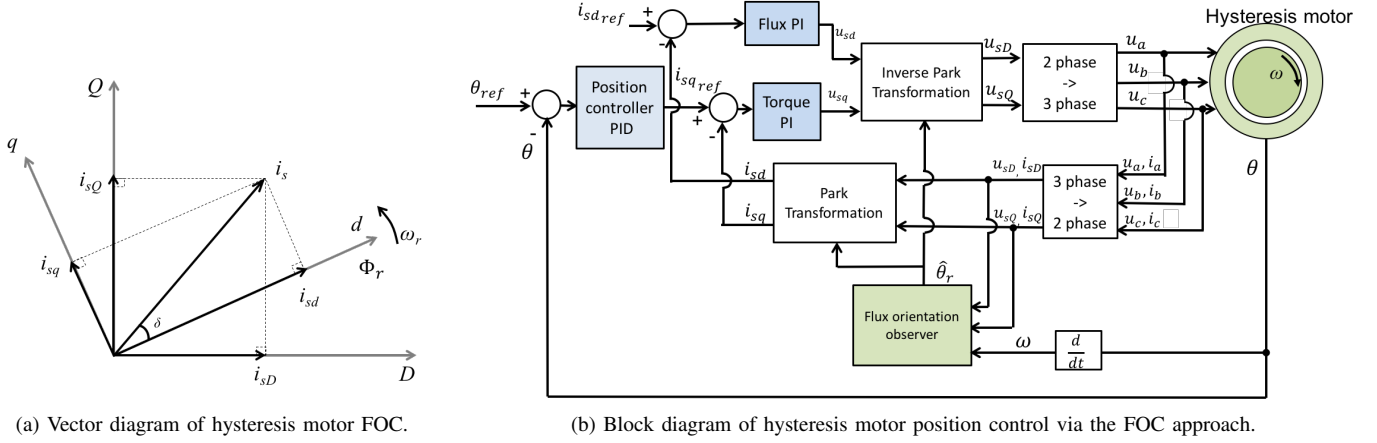


Fig. 6. Vector diagram and block diagram of hysteresis motor position control via the FOC approach.

and the rotor's mechanical angle can reach a good rotor flux angle estimation performance. One implementation of the combined flux orientation estimation is through

$$\hat{\theta} = (1 - S(|\omega_r| - \omega_r^{sw}))\theta_r + S(|\omega_r| - \omega_r^{sw})\hat{\theta}_{EMF}, \quad (18)$$

where  $|\cdot|$  is the absolute value operation,  $\omega_r$  is the rotor speed,  $\omega_r^{sw}$  is a threshold rotor speed for estimation method switching,  $\hat{\theta}_{EMF}$  is the flux angle estimation using the back-EMF method,  $\theta_r$  is the rotor's mechanical angle measured through a position sensor, and  $\hat{\theta}$  is the resultant rotor flux angle estimation.  $S(x) = 1/(1 + e^{-x})$  is the sigmoid function, which is a smooth transition function from 0 to 1 at  $x = 0$ . Through (18), an angle estimation using the mechanical angle at low speed, and using the back-EMF based estimation at high speed, can be achieved.

### C. Full-Order Observer

The third method of estimating the rotor flux orientation is by constructing a state observer for the hysteresis motor. Given the hysteresis motor state space model (9), a full-order state observer can be designed. Rewrite the system equation (9) in matrix form as

$$\dot{\mathbf{x}} = \mathbf{A}\mathbf{x} + \mathbf{B}\mathbf{u}_s, \mathbf{y} = \mathbf{C}\mathbf{x}, \quad (19)$$

where  $\mathbf{A}$ ,  $\mathbf{B}$  are the system matrices in (9),  $\mathbf{C} = [\mathbf{I}, \mathbf{0}]$  is the measurement matrix, and  $\mathbf{y} = \mathbf{i}_s = [i_{sD}, i_{sQ}]^T$  is the measurement signal. A Luenberger observer can be designed for the system as

$$\dot{\hat{\mathbf{x}}} = \mathbf{A}\hat{\mathbf{x}} + \mathbf{B}\mathbf{u} + \mathbf{L}(\mathbf{y} - \mathbf{C}\hat{\mathbf{x}}), \quad (20)$$

where  $\hat{\mathbf{x}}$  is the estimated state, and  $\mathbf{L}$  is the observer gain matrix. The observer dynamics is determined by the matrix  $\mathbf{A} - \mathbf{L}\mathbf{C}$ , and the design approach for Luenberger observers can be applied to design the observer gain  $\mathbf{L}$ . System (19) is stable in open-loop, which means  $\mathbf{L} = \mathbf{0}$  will stabilize the system. Also, the motor speed  $\omega_r$  is a parameter in the system dynamics (9). As a result, gain scheduling with  $\omega_r$  being the scheduling parameter may need to be used in the design for  $\mathbf{L}$ . The system (19) is fully observable even when the motor is operating at zero speed.

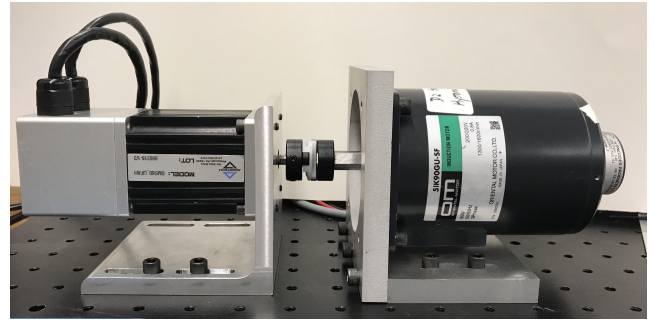


Fig. 7. Photograph of custom-made hysteresis motor with a 90 W induction motor stator connected to a brushless DC load machine.

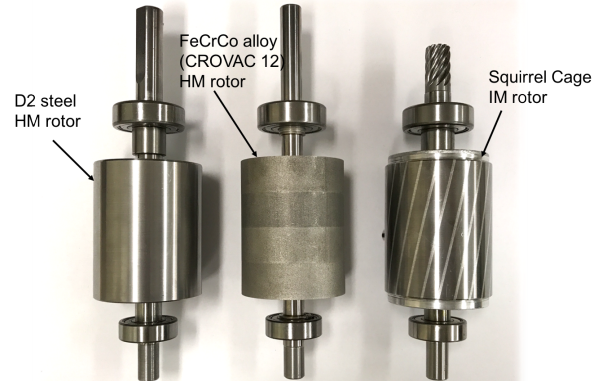


Fig. 8. Custom-made rotors for hysteresis motors. Left: D2 hysteresis rotor for Motor I. Middle: FeCrCo alloy hysteresis rotor for Motor II. Right: the original squirrel cage rotor for the induction motor.

The flux observer method provides good rotor flux angle estimation accuracy over a large speed range, and has demonstrated the best performance in the experiments among the three flux angle estimation methods. However, the estimation performance of the flux observer will significantly degrade if the model parameter errors are large. Also, this method requires full knowledge of the hysteresis properties of the rotor material, which is often not available for off-the-shelf hysteresis machines.

TABLE I  
PARAMETERS OF MOTOR I AND MOTOR II.

Parameter	Value
Motor power	90 W
Number of pole pairs	2
Rated voltage	200-220 V
Rated RMS current	0.8 A
Rotor diameter	47.5 mm
Air gap	0.4 mm
Number of turns per phase	$8 \times 80$

## V. EXPERIMENTAL TESTS

In this work, the position control system shown in Fig. 6 is experimentally tested with three hysteresis motors. Motor I and Motor II are custom-made hysteresis motors, which are manufactured by replacing the squirrel cage rotor in a regular three-phase induction motor with rotors made of different semi-hard magnetic materials. The original induction motor is a 90 W 51K90GU-SF induction motor from Oriental Motor Co., Ltd. Motor I has a rotor made of hardened D2 tool steel, which is a standard tool steel known for its resistance to wear. It also has relatively large magnetic hardness. Prior work studying D2 tool steel hysteresis motors include [4], [6], [9]. Motor II has a rotor of FeCrCo alloy, which is the CROVAC™ 12 material from Vacuumschmelze GmbH. Motor I and Motor II share the same stator construction and rotor geometry, and the only difference is in the rotor material. Fig. 7 shows a photograph of the induction motor stator with hysteresis rotor being tested, and Fig. 8 shows the custom-made rotors for Motor I and II and the original rotor for the induction motor. The parameters of Motor I and II are shown in Table I. The third hysteresis motor being tested, Motor III, is a commercial 250 W type GLLHNNB-3529 hysteresis motor from Elinco Inc. Fig. 9 shows a photograph of the Motor III, and its parameters are shown in Table II.

In the experiments, the hysteresis motors are driven by a PWM three-phase inverter manufactured by Linz Center of Mechatronics GmbH. The inverter operates with a DC bus voltage of 200 V. The three-phase currents of the motors are measured through shunt resistors of the inverter, and are fed back for current control. A slotless, brushless DC (BLDC) motor BMS60 from Aerotech Inc. is used as a load machine for the hysteresis motors, as is shown in Fig. 7 and Fig. 9. The BLDC motor is driven by a current mode linear three-phase power amplifier using PA12 from Apex Inc., where the current controllers are implemented by analog circuits. The current control for the BLDC motor has a bandwidth of 2 kHz. A sine-cosine optical encoder on the load machine is being used to measure the rotor's angular position, which can be interpolated to a resolution of  $10^5$  pulse per revolution. The signal of this encoder is also used for controlling the position of the hysteresis motor, and a stiff coupling is used to ensure stability. The controllers for the hysteresis motors are implemented in LabVIEW and are downloaded to a National Instruments PXI controller with FPGA for execution. The hysteresis motor current controller, PWM signal generation,

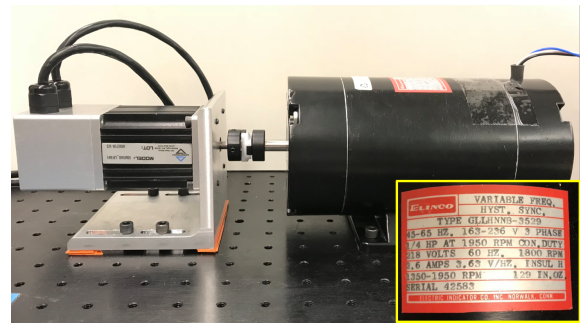


Fig. 9. Photograph of 250 W hysteresis synchronous motor from Elinco Inc.

TABLE II  
PARAMETERS OF MOTOR III.

Parameter	Value
Motor power	250 W
Number of pole pairs	2
Rated voltage	163-236 V
Rated RMS current	2.6 A

TABLE III  
ROTOR MATERIAL PROPERTIES.

Material Name	D2 steel	FeCrCo Alloy
Material chemical composition	C: 1.5%; Co: 1%; Cr: 12 %	Co: 12%; Cr: 28%; Mo: 1%
Conductivity	$8.3 \times 10^6$ S/m	$1.4 \times 10^6$ S/m
Remanence	0.85 -0.90 T	0.85 - 0.95 T
Coercitivity	1.2 - 2.3 kA/m	16-32 kA/m

encoder interpolation, and the commutation for the BLDC motor are implemented in the FPGA with a process frequency of 40 kHz, and the position controller and the flux orientation estimator are implemented in the realtime control loop with a sampling rate of 10 kHz. The hysteresis motor's current control has a bandwidth of 600 Hz.

### A. Hysteresis Measurement of Rotor Materials

This section presents the measurement and parametrization of hysteresis properties of the rotor materials for Motor I and Motor II: the D2 tool steel and the FeCrCo alloy. Table III shows the chemical, physical, and magnetic properties of the two rotor materials.

The  $B$ - $H$  curves of the two rotor materials at different excitation amplitudes are measured and are shown in Fig. 10. Reference [25] introduces the hysteresis measurement apparatus. It can be seen from Fig. 10 that the FeCrCo alloy has a larger magnetic coercivity than the D2 steel, while the saturation of FeCrCo alloy is lower than that of the D2 steel. Since the hysteresis torque generation of a hysteresis motor is proportional to the hysteresis loop area [1], the FeCrCo alloy hysteresis motor can potentially generate larger hysteresis torque than the D2 steel hysteresis motor, however it requires a larger  $H$ -field to fully utilize the hysteresis torque capability of the material.

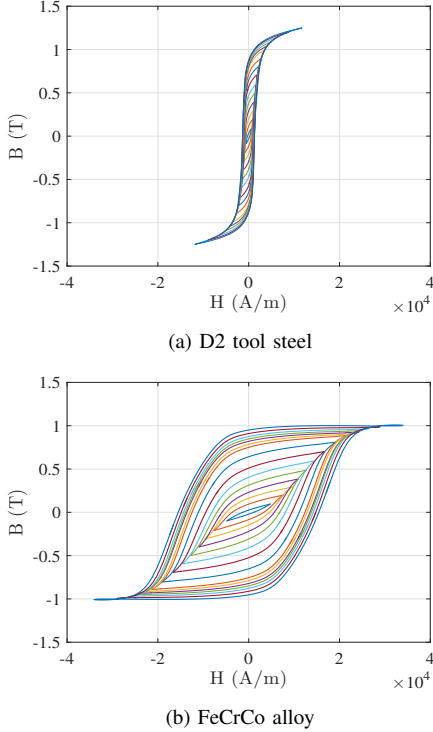


Fig. 10. Measured hysteresis properties of the D2 tool steel and the FeCrCo alloy under different sinusoidal  $B$ -field excitation amplitudes at 10Hz.

There are two parameters in the elliptical hysteresis model: the permeability  $\mu$  and the lag angle  $\delta$ . Fig. 11 shows the hysteresis parameters of D2 steel and the FeCrCo alloy under different  $B$ -field amplitude. These parameters are stored in look-up tables and are used to construct the model for hysteresis motors through Eq. (1)-(4). With the two hysteresis parameters being functions of the excitation amplitude, the magnetic saturation effect can be modeled.

### B. Open-loop Tests

The three hysteresis motors are first tested in open-loop, i.e. the position control loop for the motors is not closed. Under this test condition, the stator windings are energized with symmetric sinusoidal three-phase currents, and the motors are tested in no-load condition.

Fig. 12 presents the speed start-up curved of the three motors. In this test, the stator current zero-to-peak amplitude is 1 A for Motor I and II, and is 2.5 A for Motor III. It can be observed that the speed data of Motor II and Motor III demonstrates a larger speed oscillation amplitude than that of the Motor I, which is refereed as hunting behavior for hysteresis motors [26]. Fig. 12 also shows that the Motor I has a shorter settling time than Motor II and III. This is due to the D2 steel has a larger conductivity than the FeCrCo alloy and the rotor material for Motor III, and thus the Motor I demonstrates a larger damping than the Motor II and III.

The motors' starting torques are estimated though measuring the slope of the speed during starting up. The drag torques to the motors, including air drag and the bearing friction, are identified through the deceleration of the motor after disconnected from the power sources, and are considered

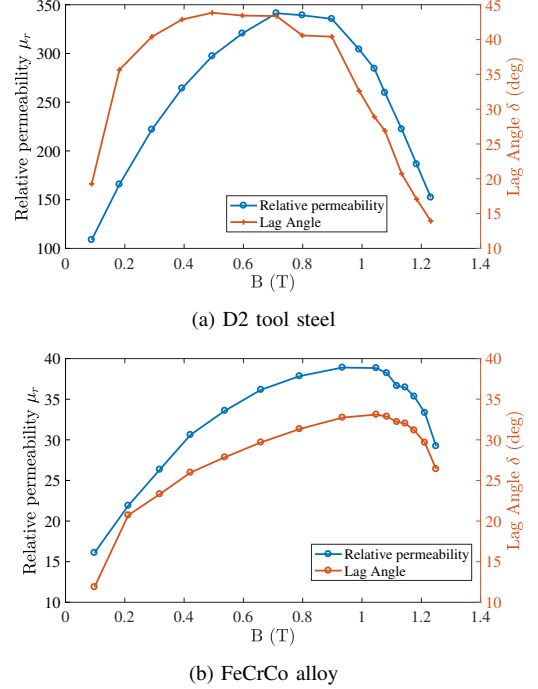


Fig. 11. Measured  $\mu_r$  and  $\delta$  of the hysteresis motor rotor materials at 10 Hz under different excitation amplitude.

in the calculation of the motor starting torques. Fig. 13 shows the torque-slip frequency relationship of the three hysteresis motors. Fig. 13(a) and (b) also presents the modeled torque calculated using the time-average hysteresis motor equivalent circuit model shown in Fig. 3, with the motor geometric parameters and hysteresis parameters of the specific rotor material being used. In Fig. 13(a) and (b), the modeled and measured torque data agree well at high slip frequency, but have a relatively large difference at low slip frequency. This is because the model assumes the hysteresis lag angle is equal to its maximum whenever the motor is running asynchronously, i.e., the slip frequency is non-zero. However when the motor slip frequency is small, the lag angle can demonstrate values smaller than the maximum lag angle, as discussed in reference [12]. Also, as is shown in Fig. 13(a) and (b), the torque of motor I increases almost linearly with the slip frequency, while the starting torque of motor II saturates to a certain value when slip frequency is high. This indicates that the dominant torque generation mechanism of Motor I is through the eddy current effects, while the dominant torque generation mechanism of Motor II is through the hysteresis effect.

Fig. 13 (c) does not show the modeled torque for Motor III since we lack the knowledge about the rotor hysteresis material property for Motor III. Comparing Fig. 13(b) and (c), it can be seen that the measured torque-slip frequency relationship of Motor III resembles that of Motor II, with both motor's torque saturate to a constant value as the slip frequency increases. This indicates that the torque generation of Motor II and III is mainly through the hysteresis effect.

Fig. 14 shows the measured torque-current relationships of the three hysteresis motors under blocked-rotor condition with a driving frequency of 20 Hz. It can be seen that the motor

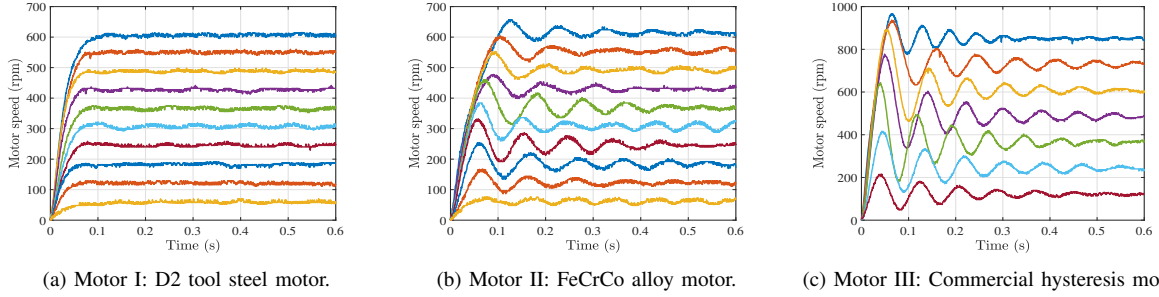


Fig. 12. Start-up speed of hysteresis motors at different reference frequencies. All speed data converge to synchronous. Peak current amplitude for Motor I and II: 1 A; peak current amplitude for Motor III: 2.5 A.

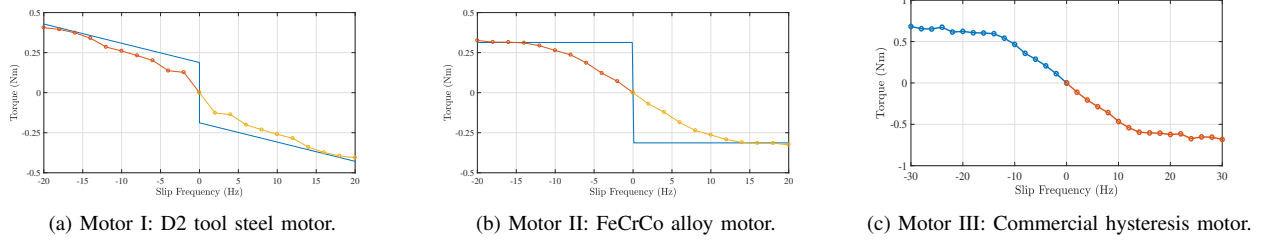


Fig. 13. Torque-slip frequency curve of hysteresis motors. Solid line: modeled torque. Marked lines: measured torque. Peak current amplitude for Motor I and II: 1 A; peak current amplitude for Motor III: 2.5 A.

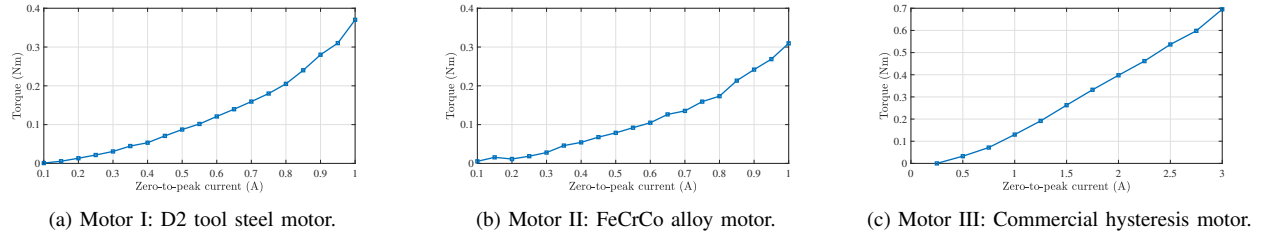


Fig. 14. Torque-current relationships of hysteresis motors at 20 Hz driving frequency.

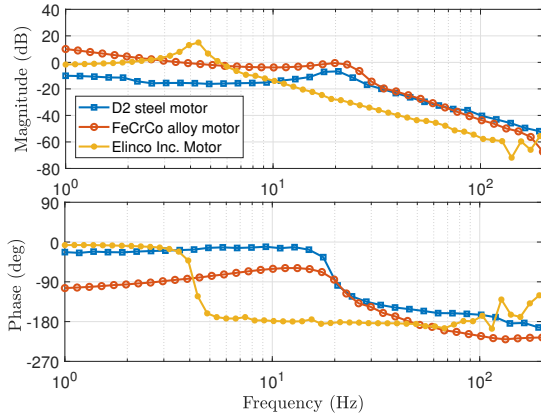


Fig. 15. Measured plant Bode plots for three hysteresis motors. Input:  $q$ -axis current amplitude; output: measured position.

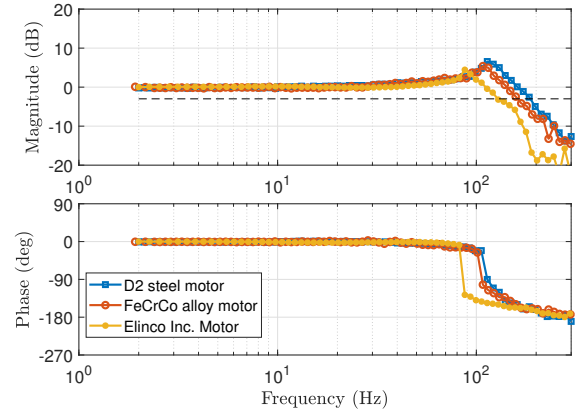


Fig. 16. Measured closed-loop Bode plots for three hysteresis motors. Input: reference position; output: measured position. The -3 dB in magnitude plot is shown as the dashed line.

torque is roughly quadratic with respect to the current.

### C. Position Closed-Loop Control

The position closed-loop control scheme shown in Fig. 6 is tested with the three hysteresis motors. The motors are first tested under no-load condition. For Motor I and Motor II, the full-order state observer method given in (19) and (20) is used for the rotor flux orientation estimation. For Motor III,

rotor flux orientation is estimated through the combination of the mechanical angle and back-EMF method, which is shown in (18). This is because the full hysteresis motor model is available for Motor I and II, and is not available for Motor III due to the lack of knowledge about the rotor material hysteresis properties.

Fig. 15 shows the measured plant frequency responses of the position control for the three hysteresis motors. In this

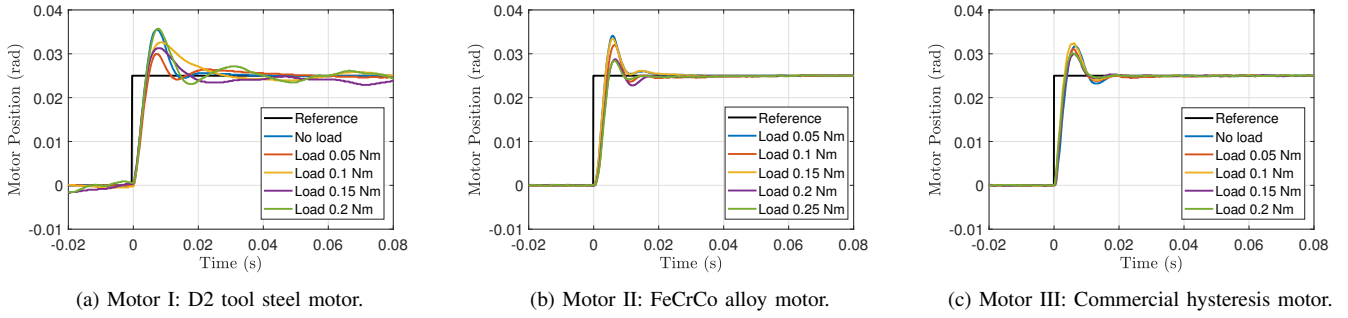


Fig. 17. Closed-loop position step response of three hysteresis motors under different load torque. The  $d$ -axis current for Motor I and II: 0.4 A. The  $d$ -axis current for Motor III: 0.6 A.

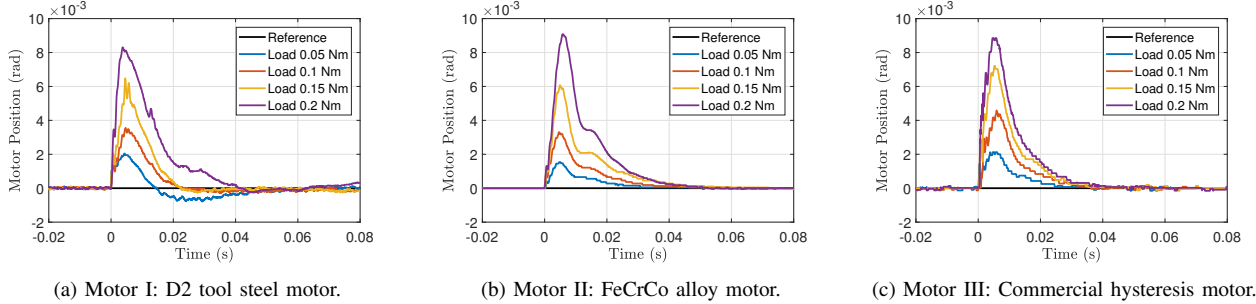


Fig. 18. Position signal of hysteresis motors under step change of disturbance torque in the positive direction. The  $d$ -axis current for Motor I and II: 0.4 A. The  $d$ -axis current for Motor III: 0.6 A.

measurement, the input signal is the  $q$ -axis current in the rotor flux-oriented frame, and the output signal is the measured rotor angular position. It can be observed in Fig. 15 that all three measured Bode plots demonstrate  $-40$  dB/dec slope at high frequency, which follows the torque-to-position relationship in a motor. The Bode plots in Fig. 15 presents zero slope at low frequency due to the bearing friction, as is discussed in reference [27]. This measurement indicates that the  $q$ -axis current is roughly proportional to the torque of the motor. It also demonstrates that the proposed flux orientation estimation approach is successful for motors with known and unknown rotor hysteresis properties.

Fig. 16 shows the measured closed-loop Bode plots for the position control systems for the hysteresis motors. Fig. 16 demonstrates that the bandwidth of the position control for the three hysteresis motors are above 130 Hz.

The hysteresis motors are also tested with load. Fig. 17 shows the measured closed-loop position step responses of the three hysteresis motors under different constant load torques, and Fig. 18 shows the hysteresis motor's position signal under a step change of the load torque. In this experiment, the load torque is applied by the BLDC load motor, which is under current control model. The load torque magnitude is determined though the load machine's current times its torque constant. It can be seen through Fig. 17 that Motor I demonstrates larger position ripple than the Motor II and III when under a constant torque larger than 0.05 Nm. This is because Motor I uses AC current to compensate the large torque, and it demonstrates torque ripple under this condition due to the high order harmonics of the motor winding. In contrast, Motor II and III are able to compensate the load torque with DC currents in their windings. This experiment shows that the hysteresis motor's position control are successful under different load

conditions, and also demonstrates that the position control for the three hysteresis motors are robust with respect to load changes.

## VI. CONCLUSIONS AND FUTURE WORK

This paper studies the position control for hysteresis motors by means of field-oriented control. A transient-time hysteresis motor model is being developed, and three methods for estimating the rotor flux orientation are proposed. Three hysteresis motors, including two custom-made hysteresis motor with D2 steel rotor and Cobalt alloy rotor and one commercial hysteresis motor, are tested and have achieved successful position control. Suggested future work includes: (i) expand the hysteresis motor model to include the rotor's magnetic remanence into the modeling to capture the history state of the rotor magnetization, (ii) explore the thrust force and/or position control for linear hysteresis motors, (iii) study sensorless FOC for hysteresis motors.

### APPENDIX A

#### TRANSIENT TIME HYSTERESIS MOTOR DYNAMICS

The transient-time dynamics of a hysteresis motor, which are shown in Fig. 4, are briefly introduced in this Appendix Section. This model is being used to derive the hysteresis motor state space model (9). In an elementary model of the hysteresis motor model, the stator flux  $\Phi_s = [\Phi_{sD}, \Phi_{sQ}]^T$ , hysteresis part rotor flux  $\Phi_{Hr} = [\Phi_{HrD}, \Phi_{HrQ}]^T$ , and eddy current part rotor flux  $\Phi_{Er} = [\Phi_{ErD}, \Phi_{ErQ}]^T$  are defined as

$$\Phi_s = L_{ls}i_s + L_m i_m, \quad (21)$$

$$\Phi_{Hr} = L_m i_m + L_{lHr} i_{Hr}, \quad (22)$$

$$\Phi_{Er} = L_m i_m + L_{lEr} i_{Er}. \quad (23)$$

The stator-side voltage balance equation is given by

$$\mathbf{u}_s = \frac{d}{dt} \Phi_s + R_s \mathbf{i}_s. \quad (24)$$

The rotor side voltage balance include two parts. The hysteresis part voltage balance relation is in the stationary frame, as

$$\mathbf{u}_{Hr} = \mathbf{0}_{2 \times 1} = \frac{d}{dt} \Phi_{Hr} + R_{Hr} \mathbf{i}_{Hr}. \quad (25)$$

The eddy current part voltage balance relationship is in the rotor-fixed frame, which is similar to that of an induction motor [23]. The equation is given by

$$\mathbf{u}_{Er} = \mathbf{0}_{2 \times 1} = \frac{d}{dt} \Phi_{Er}^r + R_{Er} \mathbf{i}_{Er}^r, \quad (26)$$

where  $\mathbf{i}_{Er}^r = [i_{Er d}^r, i_{Er q}^r]^T$  is the vector of the eddy current part of rotor current in the rotor-fixed  $d$ - $q$  frame. These equations are consistent with the equivalent circuit model of the hysteresis motor shown in Fig. 4, where the eddy current effect and hysteresis effect are in different coordinate frames.

The transform equation from the rotor-fixed  $d$ - $q$  frame to the stationary  $D$ - $Q$  frame can be done through

$$\mathbf{Z} = \mathbf{T} \mathbf{Z}^r, \quad (27)$$

where  $\mathbf{Z}$  is a dummy variable which can represent flux or current, and the transformation matrix  $\mathbf{T}$  is defined as

$$\mathbf{T} = \begin{bmatrix} \cos(\omega_r t) & -\sin(\omega_r t) \\ \sin(\omega_r t) & \cos(\omega_r t) \end{bmatrix}, \quad (28)$$

where  $\omega_r$  is the rotor speed, and  $t$  is the time. Substitute (27), (28) into (26), and writing the equation in matrix form yield

$$\begin{aligned} \frac{d}{dt} \begin{bmatrix} \Phi_{ErD} \\ \Phi_{ErQ} \end{bmatrix} &= \begin{bmatrix} \cos(\omega_r t) & -\sin(\omega_r t) \\ \sin(\omega_r t) & \cos(\omega_r t) \end{bmatrix} \left( \frac{d}{dt} \begin{bmatrix} \Phi_{Er d} \\ \Phi_{Er q} \end{bmatrix} \right) \\ &\quad + \omega_r \begin{bmatrix} -\sin(\omega_r t) & -\cos(\omega_r t) \\ \cos(\omega_r t) & -\sin(\omega_r t) \end{bmatrix} \begin{bmatrix} \Phi_{Er d} \\ \Phi_{Er q} \end{bmatrix} \\ &= - \begin{bmatrix} R_{Er} & 0 \\ 0 & R_{Er} \end{bmatrix} \begin{bmatrix} i_{ErD} \\ i_{ErQ} \end{bmatrix} - \omega_r \begin{bmatrix} -\Phi_{ErQ} \\ \Phi_{ErD} \end{bmatrix}. \end{aligned} \quad (29)$$

Equations (21)-(25) and (29) fully describe the transient dynamics of a hysteresis motor with eddy current effect being considered. There are six independent dynamic equations: (24), (25), and (29), and six independent variables. One can derive a state-space model for the hysteresis motor by selecting a set of state variables, and eliminating all other variables. Many different state variable selection can be made, and the model represents the same dynamics. By selecting a set of state variables as  $\mathbf{x} = [i_s^T, \Phi_{Hr}^T, \Phi_{Er}^T]^T$ , the state-space model (9) can be derived.

#### ACKNOWLEDGMENT

We thank ASML for supporting this work. We thank Dietmar Andessner at the Linz Center of Mechatronics, GmbH for his help with the hysteresis property measurements. We thank Prof. James Kirtley at MIT for the valuable discussion.

#### REFERENCES

[1] B. R. Teare, "Theory of hysteresis-motor torque," *Electrical Engineering*, vol. 59, no. 12, pp. 907–912, 1940.

[2] H. C. Roters, "The hysteresis motor-advances which permit economical fractional horsepower ratings," *Trans. of the American Institute of Electrical Engineers*, vol. 66, no. 1, pp. 1419–1430, 1947.

[3] R. Nasiri-Zarandi, M. Mirsalim, and A. Tenconi, "A novel hybrid hysteresis motor with combined radial and axial flux rotors," *IEEE Trans. on Industrial Electronics*, vol. 63, no. 3, pp. 1684–1693, 2016.

[4] M. Noh, W. Gruber, and D. L. Trumper, "Hysteresis bearingless slice motors with homopolar flux-biasing," *IEEE/ASME Trans. on Mechatronics*, vol. 22, no. 5, pp. 2308–2318, 2017.

[5] M. Copeland and G. Slemon, "An analysis of the hysteresis motor i-analysis of the idealized machine," *IEEE Trans. on Power Apparatus and Systems*, vol. 82, no. 65, pp. 34–42, 1963.

[6] M. Imani Nejad, "Self-bearing motor design and control," Ph.D. thesis, Massachusetts Institute of Technology, 2013.

[7] A. Darabi, H. Tahanian, S. Amani, and M. Sedghi, "An experimental comparison of disc-type hysteresis motors with slotless magnetic stator core," *IEEE Trans. on Industrial Electronics*, vol. 64, no. 6, pp. 4642–4652, 2017.

[8] K. Rajagopal, "Design of a compact hysteresis motor used in a gyroscope," *IEEE Trans. on Magnetics*, vol. 39, no. 5, pp. 3013–3015, 2003.

[9] L. Zhou, M. I. Nejad, and D. L. Trumper, "One-axis hysteresis motor driven magnetically suspended reaction sphere," *Mechatronics*, vol. 42, pp. 69–80, 2017.

[10] M. Zare and A. Halvaei Niasar, "A novel sensorless vector control of high-speed hysteresis motor drive," *Journal of Power Electronics & Power Systems*, vol. 2, no. 3, pp. 1–7, 2013.

[11] L. Zhou, W. Gruber, and D. L. Trumper, "Position control for hysteresis motors: A field-oriented control approach," in *IEEE International Electric Machines and Drives Conference*, 2017.

[12] D. O'Kelly, "Eddy-current and hysteresis effects in rotating machines," *Proceedings of the Institution of Electrical Engineers*, vol. 116, no. 3, pp. 391–394, 1969.

[13] M. A. Rahman, "Analytical models for polyphase hysteresis motor," *IEEE Trans. on Power Apparatus and Systems*, no. 1, pp. 237–242, 1973.

[14] D. O'Kelly, "Theory and performance of solid-rotor induction and hysteresis machines," in *Proceedings of the Institution of Electrical Engineers*, vol. 123, no. 5. IET, 1976, pp. 421–428.

[15] S. Miyairi and T. Kataoka, "A basic equivalent circuit of the hysteresis motor," *Elect. Engng. Japan (USA)*, vol. 85, pp. 41–50, 1965.

[16] —, "Analysis of hysteresis motors considering eddy current effect," *Electrical Engineering in Japan*, vol. 86, no. 6, p. 67, 1966.

[17] T. Kataoka, "Unified analysis of solid rotor induction and hysteresis motors," *Electrical Engineering in Japan*, vol. 95, no. 3, pp. 60–67, 1975.

[18] S. Mirimani, A. Vahedi, M. R. Ghazanchaei, and A. Baktash, "Electromagnetic analysis of hysteresis synchronous motor based on complex permeability concept," *Iranian Journal of Electrical and Electronic Engineering*, vol. 9, no. 2, pp. 88–93, 2013.

[19] R. Nasiri-Zarandi and M. Mirsalim, "Finite-element analysis of an axial flux hysteresis motor based on a complex permeability concept considering the saturation of the hysteresis loop," *IEEE Trans. on Industry Applications*, vol. 52, no. 2, pp. 1390–1397, 2016.

[20] S. Rabbi, M. P. Halloran, T. LeDrew, A. Matchem, and M. A. Rahman, "Modeling and v/f control of a hysteresis interior permanent-magnet motor," *IEEE Trans. on Industry Applications*, vol. 52, no. 2, pp. 1891–1901, 2016.

[21] H.-K. Kim, H.-K. Jung, and S.-K. Hong, "Finite element analysis of hysteresis motor using the vector magnetization-dependent model," *IEEE Trans. on magnetics*, vol. 34, no. 5, pp. 3495–3498, 1998.

[22] T. A. Lipo, *Vector control and dynamics of AC drives*. Oxford university press, 1996, vol. 41.

[23] R. Marino, P. Tomei, and C. M. Verrelli, *Induction motor control design*. Springer Science & Business Media, 2010.

[24] T. Kataoka, T. Ishikawa, and T. Takahashi, "Analysis of a hysteresis motor with overexcitation," *IEEE Trans. on Magnetics*, vol. 18, no. 6, pp. 1731–1733, 1982.

[25] D. Andessner, R. Kobler, J. Passenbrunner, and W. Amrhein, "Measurement of the magnetic characteristics of soft magnetic materials with the use of an iterative learning control algorithm," in *2011 IEEE Vehicle Power and Propulsion Conference*, 2011, pp. 1–6.

[26] C. K. Truong, "Analysis of hunting in synchronous hysteresis motor," Master's thesis, Massachusetts Institute of Technology, 2004.

[27] J. Y. Yoon and D. L. Trumper, "Friction modeling, identification, and compensation based on friction hysteresis and dahl resonance," *Mechatronics*, vol. 24, no. 6, pp. 734–741, 2014.